Atom Indonesia Vol. 36 No. 2 (2010) 77 - 85

The Role of X–Ray Diffraction for Analyzing Zr-Sn-Nb-Fe Alloys as Power Reactor Fuel Cladding

Sugondo*

Center for Nuclear Fuel Element Technology, National Nuclear Energy Agency, Puspiptek, Serpong, Tangerang 15314, Indonesia

ARTICLE INFO

Article history:
Received 20 November 2009
Received in Revised form 31 August 2010
Accepted 31 August 2010

Keywords:
Power reactor
Fuel cladding
Alloy
Pellet
Heat treatment
Hardness
Microstructure

ABSTRACT

Synthesis of Zr–1%Nb–1%Sn–1%Fe alloy is undertaken in order to develop fuel cladding alloy at high burn-up. Powder specimens of Zr-Sn-Nb-Fe alloy were prepared and then formed into pellets with a dimension of 10 mm in height × 10 mm in diameter using a pressure of 1.2 ton/cm^2. The 5 gram green pellets were then melted in an arc furnace crucible under argon atmosphere. The pressure in the furnace was set at 2 psi and the current was 50 A. Afterwards, the ingots were heated at a temperature of 1100 °C for 2 hours and subsequently quenched in water. The ingots then underwent annealing at temperatures of 400 °C, 500 °C, 600 °C, 700 °C, and 750 °C for 2 hours. The specimens were analyzed using X-ray diffraction in order to construct diffractograms. Results of the diffraction patterns were fitted with data from JCPDF (Joint Committee Powder Diffraction File) to determine the type of crystals in the elements or substances. The greater the crystallite dimension, the smaller the dislocation density. Agreeable results for hardening or strengthening were obtained at annealing temperatures of 500 °C and 700, whereas for softening or residual stress at 600 °C and 750 °C. The nucleation of the secondary phase precipitate (SPP) was favourable at annealing temperatures of 400 °C, 500 °C, and 700 °C. For Zr–1%Nb–1%Sn–1%Fe alloy with annealing temperatures between 400 °C to 800 °C, precipitates of Fe_2Nb, $ZrSn_2$,FeSn, SnZr, $NbSn_2$, $Zr_{0.68}Nb_{0.25}Fe_{0.08}$, $Fe_2Nb_{0.4}Zr_{0.6}$, $Fe_{37}Nb_9Zr_{54}$, and ω–Zr were observed. Satisfactory precipitate stabilization was achieved at annealing temperature of 800 °C, growth of precipitates at temperature between 500 °C to 600°C, and minimization of precipitate size at 700 °C.

© 2010 Atom Indonesia. All rights reserved

INTRODUCTION

Zirconium alloy (Zircalloy) is the main metal component used in the nuclear industry. In the nuclear reactors, Zircalloy is used as cladding of the fuel as protection against coolant, containment of fission gas products, heat transfer material, and structural material. For these purposes, Zircalloy must possess good mechanical properties, excellent corrosion resistance, and low neutron absoprtion. For example, Zircaloy–2 (Zr–1.7%Sn–0.2%Fe–0.15%Cr–0.08%Ni) is used in boiling water reactor (BWR) and Zircaloy–4 (Zr–1.7%Sn–0.24%Fe–0.13%Cr) for pressurized water reactor (PWR), with the respetive cladding temperatures of 390 °C for BWR and 349 °C for PWR [1].

To enhance reactor efficiency, the cumulative power must be increased. The main issue is the cladding materials Zircaloy-2 and Zircaloy-4 will not be able to stand a high burn-up condition. Other cladding material that will serve the purpose is Zirlo (Zr-1%Nb-1%Sn-0.1%Fe) [2]. Addition of iron as an alloying element at concentrations between 0.2 – 1% into the Zr-1%Sn alloy is found to decrease the corrosion rate[3] and the same prevails for the Zr-1%Nb alloy.

The development of Zr-Sn-Nb-Fe alloy is mainly as material for fuel cladding at high burn-up. The superior properties of the alloy are as follows. Firstly, coolant temperature can be increased. Power efficiency can easily be attained if the operating temperature is raised to 400 – 600 °C. Secondly, the concentration of lithium (Li) in coolant can be higher. In the operation of a PWR reactor, the pH must be strictly maintained because it is essential in determining the oxide solubility. Reactor operation

* Corresponding author.
E-mail address:.sugondo@batan.go.id (Sugondo)

at higher pH (~7.4) is an effective solution to coolant radioactivity. However, higher pH is actually desirable from the radiation exposure point of view (rate of dissolution of oxide/crud will decrease) but it can result in corrosion/crack on the tubing material of the steam generator and damage/corrosion on the fuel cladding material. Thirdly, reduced creep and growth due to irradiation are obtained. Fourthly, hydrogen pick-up is reduced. Fifthly, the alloy has higher corrosion resistance than Zircaloy-2 (Zry-2) and Zircaloy-4 (Zry-4). These advantages can be observed following the post irradiation examination (PIE) of irradiation products with a burn-up of 70,000 MWd/Te [4].

Currently, corrosion characteristics of Zircaloy have become the main issue in fuel technology for light water reactors (LWRs). Resistance to corrosion of the reactor and structural materials restricts fuel economy improvement with regard to the increase in heat flux, coolant temperature, and fuel cycle. The challenge on fuel performance is focused on optimizing the chemical composition and the microstructures of commercial alloys (Zry-2), (Zry-4), Zr-1%Nb, and Zr-2.5%Nb. The corrosion resistance of PWR cladding (Zry–4) will be enhanced if the size of the secondary phase particles (SPP) is greater than one-tenth of a micrometer and the tin (Sn) content is lower than the specification. Recent studies, however, show that the maximum corrosion resistance is attained at an SPP with a size smaller than one-tenth of a micrometer for Zr-1%Nb, Zr-2.5%Nb, and Zirlo. Small SPP size is also beneficial in reducing the nodular corrosion in BWRs.

The present development of fuel cladding materials is directed toward optimization of the material composition: E110 (Zr-1%Nb), E635 (Zr-1.2%Sn-1.0%Nb-0.35%Fe), and Zirlo (Zr-1.0%Sn-1.0%Nb-0.1%Fe). This study is carried out to perform characterization of Zr-1.0%Sn-1.0%Nb-1.0%Fe alloy using X-ray diffraction, which includes: phases, crystallite size, dislocation density, yield strength, and precipitates.

THEORY

Zirconium and Its Alloys

Zirconium possesses two crystal structures (allotropy), α-phase (hexagonal closepacked) and β-phase (body centred cubic). The transformation of zirconium metal from α to β-phase occurs at 863 ± 5 °C, with a melting point of 1852 ± 2 °C. At room temperature, zirconium metal (hcp) has lattice distances of a = 3.23 Å and c = 5.15 Å. The presence of alloying elements and or the increase in temperature can result in a higher c/a ratio [5]. The alloying elements can stabilize the two different phases [6], for instance:

α-phase stabilizer: Al, Sb, Sn, Be, Pb, Hf, N, O, Cd
β-phase stabilizer: Fe, Cr, Ni, Mo, Cu, Nb, Ta, V, Th, U

The mechanism of the role of the alloy is as follows. Zircaloy is used as cladding material that interacts with fission products and reactor coolant. Reaction with zirconium will lead to corrosion of the material. Consequently, the zircaloy has to fulfil the electron configuration theory through the formation of intermetallic compounds to repel the electron clouds of the oxygen and the hydrides. These intermetallic compounds could be in the form of solid solution and precipitates.

Effects of Alloying Elements on Mechanical Properties and Oxidation Resistance

Tin (Sn)

Sn is an α-phase stabilizer. In the α and β phases, it can form substitutional solid solution [7]. Sn can improve mechanical properties by solid solution hardening. The increase of corrosion in hot water medium is due to the formation of precipitates of ZrSn, Zr_4Sn, Zr_3Sn_2, and Zr_5Sn_3.

Sn is initially added at a concentration of 1.2 – 1.7% to enhance the resistance to corrosion by lessening the effect of nitrogen in decreasing the corrosion resistance. With a better control of the process parameters, which includes decreasing the nitrogen content, the concentration of Sn in zirconium alloy for PWRs can be reduced. Sn helps to enhance corrosion resistance in hot water, and to improve mechanical strength of the alloy.

Niobium (Nb)

Monotectoid transformation occurs at a temperature of 620 °C with a concentration of 18.5 at% Nb [7]. Nb at a concentration of 0.1 – 0.5% is found in the matrices, while Nb at a concentration greater than 0.5% is found in the precipitates [8]. However, it is reported that Nb at a concentration of 0.1% is also found in the precipitates.

Corrosion resistance of Zircaloy-4 can be enhanced by the addition of alloying elements, such as Nb. It is asserted that addition of a small amount

of Nb (around 0.05 – 0.2%) can reduce the weight gain to a significant level, whereas addition at a concentration greater than 0.2% can increase the weight gain. This result was based on autoclave testing in steam at 300 °C and 10.3 MPa for 300 days. It is also revealed that addition of Nb can improve the resistance to corrosion [8]. In general, Nb helps to increase hardness at high temperature, reduce the eutectoid temperature, and improve the resistance to corrosion.

Iron (Fe)

New materials are invented, for example, Zirlo and E635 which exhibit superior characteristics than Zircaloy-4 and Zircaloy-2 during experimental testing in the corresponding reactor type. Out-of-pile testing at a temperature up to 427 °C has been compared with the irradiation. The results indicate that Zirlo delivers a better performance than Zry-4. The rate of hydriding and the increase of oxide thickness for Zirlo are less than those for Zry-4 [9]. The effects of cooling from tempered temperature with respect to hydride reorientation, particularly in radial direction, are under investigation. The tempered temperature is found to have some influence on the re-orientation of the hydrides. Heat treatment has significant effects on the resistance to corrosion. At certain heating temperature (500 °C), excellent resistance to corrosion is observed. In general, Fe helps to increase the ductility and strength, and form multi precipitate compounds that can increase burn-up.

Heat Treatment and Microstructures

Homogenization of the β-phase causes all second phase particles to dissolve completely [7], but causes significant grain growth. After annealing at 1050 °C for 30 minutes, the size of the grains can reach a few millimeters. During quenching in water, the shape of the β grains transform from α needle to bainite, due to the slow cooling rate and the ingot size. The β-eutectoid elements precipitate at the grain boundaries of the needle structure. Ingots that have undergone rapid β-quenching are used as a reference state for the next processes. Cold working and intermediate recrystallization are performed to further control the distribution of the precipitate size.

X-Ray Diffraction

Strain and Residual Stress

Strain and residual stress can be identified using X-ray diffraction through the plot of intensity versus Bragg angle (θ) of the X-ray spectrum, called diffractogram. Peaks in a diffractogram possess two characteristics when compared with peaks of a single crystal, which are peak shift and broadening [10].

The peak shift can be explained as follows. If a material receives a tensile force (F) over an area A, then it will first experience plastic strain (ε). Given the length (L), the strain toward the tensile direction (ε_y) is the ratio of the change in length ($L_1 - L_0$) with respect to the initial length (L_0).

$$\varepsilon_y = \Delta L/L_0 = (L_1 - L_0)/L_0 \quad (1)$$

The basic equation for elasticity is given by stress (σ) which is proportional to the Young's modulus (E) and elastic strain (ε). This correlation in the tensile direction (y) is:

$$\sigma_y = E\,\varepsilon_y \quad (2)$$

For material with a cylindrical shape having a diameter (D) and experiencing strain toward the (Z) direction, i.e. the tangential direction, the elastic strain is given by:

$$\varepsilon_z = (D_1 - D_0)/D_0 \quad (3)$$

where D_0 is the initial diameter and D_1 is the diameter during straining ε_z. If the strain is homogenous or isotropic, then the strain toward the tangential direction (Z) is equal to the strain toward the radial direction (X). The correlation with the strain toward the axial direction (Y) is written as follows:

$$\varepsilon_z = \varepsilon_x = -\nu\varepsilon_y \quad (4)$$

It should be noted that strain, regardless of its size, only has slight effect on the crystal lattice distance (d) and the strain toward the (Z) direction is:

$$\varepsilon_z = (d_1 - d_0)/(d_0) \quad (5)$$

Substituting into equation (2), we obtain:

$$\sigma_y = (-E/\nu)\,(d_1 - d_0)/(d_0) = (-E/\nu)\,(\Delta d)/(d_0) \quad (6)$$

where ν is the Poisson's ratio and E is the yield strength. Relating this with X-ray diffractogram (intensity vs Bragg angle), Δd is the maximum peak shift of the diffractogram. σ_y is called the residual microstress and ε_y is the residual macrostrain toward the uni-axial direction.

The peak broadening of the diffractogram is caused by heterogeneous/inhomogeneous residual strain due to the formation of subgrains, curved grains, and the presence of dislocations. The residual stress is caused by the stress in the grains. The broadening of the peaks (B), Bragg angle (θ), and lattice distance (d) yield the following correlation:

$$B = (-2\, d \tan\theta)/(d_0) \quad (7)$$

The value of (Δd/d) takes into account tensile and compression. Based on equation (2), we obtain:

$$\sigma = (EB)/(4 \tan\theta) \quad (8)$$

where the (B)/(4 tan θ) segment is the residual microstress.

From the arguments above, a hypothesis is proposed that when there are shift and broadening of the diffractogram peaks, then there will be changes in the crystal lattice distance, residual stress, and residual grain strain having an anisotropic behaviour.

Crystallite Size and Yield Strength

In general, the XRD peak profiles broaden as a result of the very small crystallite size - less than the grain size, the presence of microstrain due to dislocations, and the stacking faults. Therefore, peak broadening can be used for analysis of materials. The peaks of the XRD are the reflections of various lattice planes which are the characteristics of materials. The diffractogram shape (peak profile) is influenced by instrument and sample shape.

Correction for the peak broadening due to instrument is the main step to obtain the actual peak of the material. Peak broadening due to instrument (b) is defined as the ratio of peak area (A) and maximum intensity (I_0) when there is no peak broadening present. The peak broadening due to instrument (b) is a function of Bragg angle, θ, formulated as follows [11]:

$$b^2 = U \tan^2\theta + V \tan\theta + W \quad (9)$$

where U, V, and W are constants. This model precludes a small divergence angle, i.e. 2θ smaller than 30°. b^2 is obtained by plotting $(FWHM)^2$ vs tanθ to yield a regression polynomial equation to give the values of U, V, and W. Therefore, correction of peak broadening due to instrument can be determined.

Peak broadening from observation (B) is corrected with the peak broadening due to instrument (b, producing corrected peak broadening (β) given by the formula below [11]:

$$\beta = B - (b^2/B) \quad (10)$$

Peak broadening is also related to the crystallites (D) and microstrain (ε). The following formula [9] shows the correlation between peak broadening (B), crystallite size (D), microstrain (ε), Bragg angle (θ), and wavelength (λ) in (Å) unit.

$$(\beta\cos\theta/\lambda)^2 = (1/D)^2 + (4\varepsilon\sin\theta/\lambda)^2 \quad (11)$$

Based on this equation, a plot of $(\beta \cos\theta/\lambda)^2$ vs $(\sin\theta/\lambda)^2$ can be obtained, with an intercept of $(1/D^2)$ and a slope of $16(\varepsilon)^2$.

Afterward, the dislocation density (ρ) can be computed using the following formula [12]:

$$\rho = 3\eta/(D)^2 \quad (12)$$

where η is a constant whose value approaches 1 and D is the crystallite size. After the dislocation density is known, the yield strength (Y_s) can be determined using the following formula [12]:

$$Y_s = 274.54 + 4.963 \times 10^{-6} \sqrt{\rho} \quad (13)$$

The unit of Y_s is MPa and that of ρ is m/m^3 or $1/m^2$.

EXPERIMENTAL METHODS

Preparation of Alloys

Zr, Sn, Nb, and Fe powders are each weighed to obtain an alloy composition of Zr-1%Sn-1%Nb-1%Fe. The powders are blended in a mixer for 150 minutes, and then pressed at a pressure of 1.2 ton/cm^2 to obtain pellets with a size of 10 mm in height × 10 mm in diameter. The pellets from this step are called raw pellets. Afterward, 5 g of raw pellets are melted in an arc furnace using a copper crucible under argon gas atmosphere. The pressure in the furnace chamber is 2 psi and the arc current is 50 A. The yield, Zr-Sn-Nb-Fe alloy ingot, is then heated at a temperature of 1100°C for 2 hours followed by rapid quenching in water**.** The ingot is subsequently cut with a diamond blade to obtain a size of 5 × 2 × 10 mm**.** The specimen cuts are divided into two groups for rolling and annealing treatments. The first group is rolled with degrees of deformation of 0%, 20%, 40% and 60%. Meanwhile, the second group is annealed at temperatures of 400°C, 500 °C, 600 °C, 700 °C, 750 °C and 800 °C for 2 hours. Chemical analysis is performed using EDX (*Energy Dispersive X-Ray*). Metallography testing is carried out using optical microscope, and hardness using Vickers. Sampling is based on a mode system, where in this study three samplings are used.

Analysis using X-Ray Diffraction

The specimens are polished using grid mesh up to 1200 to remove the oxides that are formed during the process. Diffractograms are obtained using JEOL, DX-GERP-12 with the following specifications: Tube = Cu; Filter = Ni; Voltage = 36 KV; Current = 20 MA; Speed = 2°/min. The results of the diffraction patterns are matched with the data in JCPDF (*Joint Committee Powder Diffraction File*) to obtain the type of crystal of elements or compounds.

RESULTS AND DISCUSSION

Crystallite Size and Yield Strength

The diffractograms obtained from X-ray diffraction can be seen in Fig. 1-7. Based on the data in JCPDS (*Joint Committee of Powder Diffraction Standard*), number 05-0665 has matching diffraction angles(Bragg angles), as marked in Fig. 1-7. Hence, it can be concluded that the crystal structure of the synthesized alloy is α–Zr, which is hexagonal with a = 3.232 Å and c = 5.147 Å.

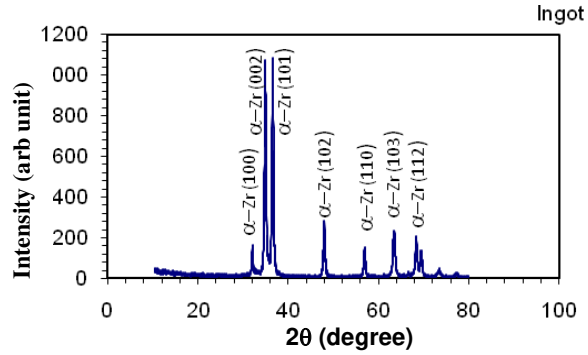

Fig. 1. X-ray diffraction pattern for Zr-Sn-Nb-Fe alloy ingot (Zr-A).

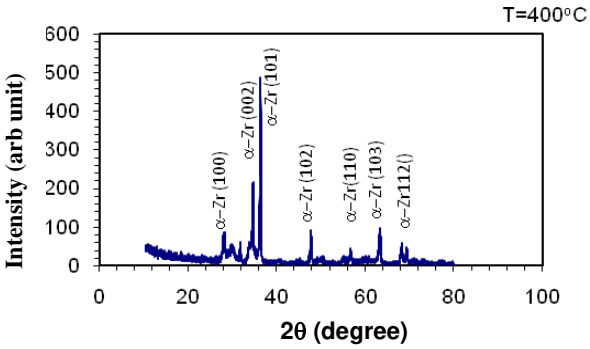

Fig. 2. X-ray diffraction pattern for Zr-Sn-Nb-Fe alloy, annealed at 400 °C (Zr-400) for 2 hours.

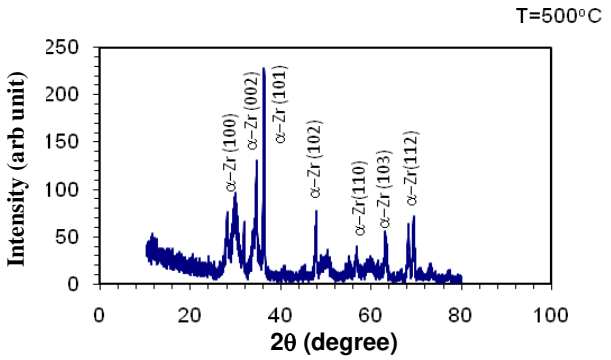

Fig. 3. X-ray diffraction pattern for Zr-Sn-Nb-Fe alloy, annealed at 500 °C (Zr-500) for 2 hours.

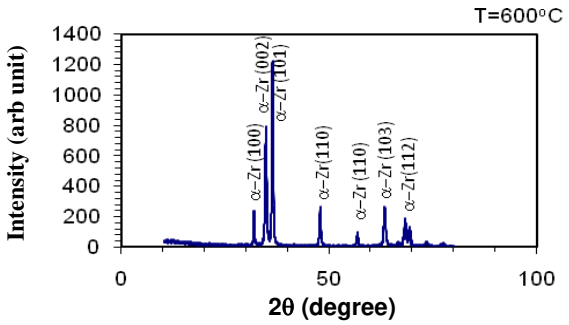

Fig. 4. X-ray diffraction pattern for Zr-Sn-Nb-Fe alloy, annealed at 600 °C (Zr-600) for 2 hours.

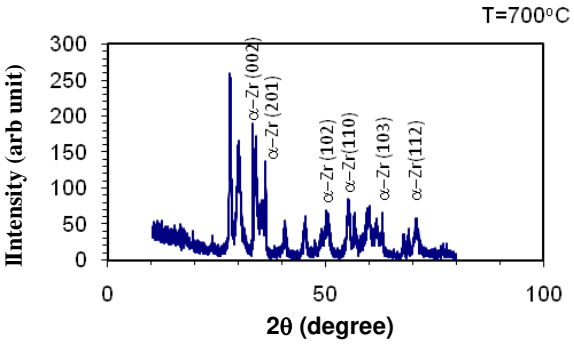

Fig. 5. X-ray diffraction pattern for Zr-Sn-Nb-Fe alloy, annealed at 700 °C (Zr-700) for 2 hours

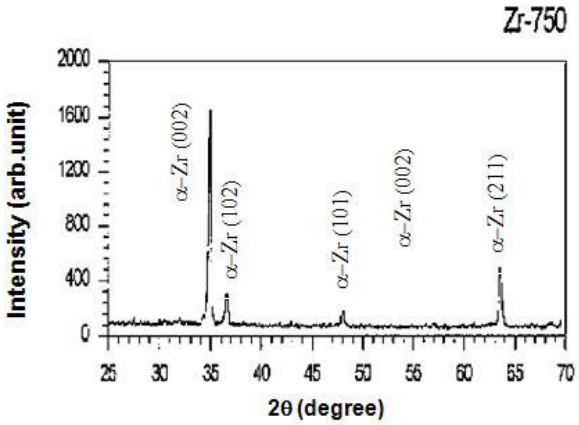

Fig. 6. X-ray diffraction pattern for Zr-Sn-Nb-Fe alloy, annealed at 750 °C (Zr-750) for 2 hours.

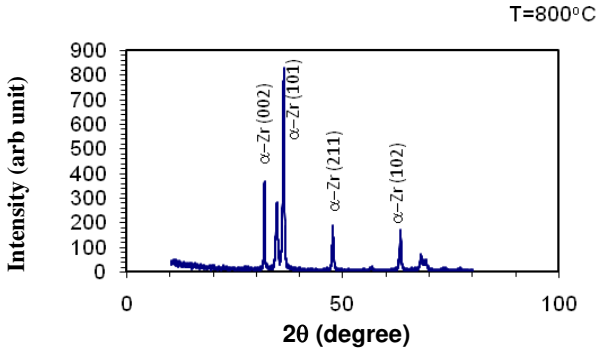

Fig. 7. X-ray diffraction pattern for Zr-Sn-Nb-Fe alloy, annealed at 800 °C (Zr-800) for 2 hours.

Correction for peak broadening of instrument using equation (10) is done to determine b^2 as a function of Bragg angle for each peak. Determination of b^2 is performed by plotting $(FWHM)^2$ versus tanθ and a regression as shown in Table-1 is obtained. Based on this regression, the value of b^2 can be established. The b^2 is then inserted into equation (2) to correct the peak broadening. From here, a plot of $(\beta \cos \theta/\lambda)^2$ versus $(\sin\theta/\lambda)^2$ is obtained. The regression from the plot matches that of equation (11), so the intercept is $(1/D)^2$ as crystallite size (sub-grain) and the slope is $(4\varepsilon)^2$, where ε is the microstrain. The value of D can be used to determine the dislocation density (ρ) using equation (12) and the yield strength using equation (13). The crystallite size, microstrain, dislocation density, and yield strength are given in Table 2.

Microstrain (ε)

From Table 1, it is shown that the microstrain in specimen from rapid quenching (Zr-A) is 2.50 %, in specimen from annealing at 500 °C (Zr-500) 13.85 %, in specimen from annealing at 600 °C (Zr-600) 3.74 %, in specimen from annealing at 700 °C (Zr-700) 4.02 %, and in specimen from annealing at 750 °C (Zr-750) 2.38 %. The microstrain in specimen from rapid quenching and that from annealing at 750 °C are almost the same, which are 2.50 % and 2.38 % respectively. The data shows that the low microstrain might result from the formation of solid solution from the alloying metals, because during melting of the alloy, precipitation and stacking faults might occur which could result in high microstrain value. The specimen from annealing at 500 °C has a microstrain of 13.85 %. It can be seen from the peaks in the diffractogram that the specimen from annealing at 500 °C has 10 peaks (2θ = 31.700, 33.900, 34.550, 36.250, 47.650, 56.600, 63.150, 68.050, and 69.150 degrees, Fig. 7). The result shows that more crystal seeds are obtained compared to other heat treatments. It is suggested that the crystal seeds are precipitates, which might hinder grain growth. As a result, the grain seeds do not grow in an equiaxial direction but pointing toward a certain direction (elongation). Thus, annealing at 500 °C presents satisfactory results for precipitation or randomization of the crystals. The microstrain for annealing at 600 °C is 3.74%, which increases slightly compared to that of the specimen from rapid quenching, which is 2.50%. The diffractogram of the specimen has 8 peaks (2θ = 31.600, 34.450, 47.550, 56.500, 63.150, 68.100, 69.150 degrees, Fig.-8) which is the same with the specimen from rapid quenching (2θ = 31.600, 34.400, 47.550, 56.450, 63.000, 67.950, 69.050 degrees, Fig.-5). So, annealing at 600 °C is favorable for grain growth. Meanwhile the increase of microstrain compared to specimen from rapid quenching might largely be due to stacking faults, since there is no reduction and addition of peaks in the diffractogram, which means that there is no disappearance or appearance of seeds. Specimen from annealing at 750 °C has a microstrain of 2.38 %. The diffractogram of this specimen has 4 peaks (2θ = 34.800, 36.500, 48.000, 47.550 degrees, Fig.-10), half of that in the diffractogram for specimen from rapid quenching. This means that annealing at this temperature is favorable for the growth of equiaxed grains, as there are no stacking faults or precipitates which can lead to small microstrain.

Table 1. Correlation of peak broadening as a function of Bragg angle

No.	Specimen	Regression of corrected broadening peak of instrument	
		Corrected FWHM (b^2)	tan (θ) function
1	Zr-A	b^2 =	0.674 $\tan^2\theta$ – 0.5632 tan θ + 0.3
2	Zr-500	b^2 =	0.7601 $\tan^2\theta$ –01.3523 tan θ+ 0.7
3	Zr-600	b^2 =	2.3547 $\tan^2\theta$ – 1.7965 tan θ + 0.5
4	Zr-700	b^2 =	1.0882 $\tan^2\theta$ – 1.3015 tan θ + 0.6
5	Zr-750	b^2 =	2.3775 $\tan^2\theta$ – 1.982 tan θ + 0.5

Table 2. Microstrain, crystallite size, dislocation density, and yield strength*

Specimen	$(4\varepsilon)^2$	$(1/D)^2$	ε	D (Å)	ρ (m/m^3)	Y_s (MPa)
Zr-A	0.01	4.00E-03	0.0250	15.8114	1.20E+16	818.21
Zr-500	0.3069	8.00E-03	0.1385	11.1803	2.40E+16	1043.40
Zr-600	0.0224	9.00E-04	0.0374	33.3333	2.70E+15	532.43
Zr-700	0.0259	8.00E-03	0.0402	11.1803	2.40E+16	1043.40
Zr-750	0.0091	2.00E-04	0.0238	70.7107	6.00E+14	396.11

* Zr-A = specimen from rapid quenching; Zr-500, Zr-600, Zr-700, Zr-750 = specimens from annealing at 500, 600, 700, 750 °C; ε = microstrain; D = cystallite size; ρ = dislocation density; Y_s = yield strength.

Crystallite Size (D)

From Table 1, cystallite size data are obtained which is 15.81 Å for specimen from rapid quenching, 11.18 Å from annealing at 500 ^{o}C, 33.33 Å from annealing at 600 ^{o}C, 11.18 Å from annealing at 700 ^{o}C and 70.71 Å from annealing at 750 ^{o}C. Compared to specimen from rapid quenching, specimens from annealing at 600 ^{o}C and 750 ^{o}C possess greater crystallite size with increasing annealing temperature. The largest crystallite size is obtained at annealing at 750 ^{o}C, which is 70.71 Å. It turns out that the number of peaks on the diffractogram for rapid quenching is 8 peaks (Fig. 5) is the same with that from annealing at 600 ^{o}C (Fig. 8), but for annealing at 750 ^{o}C the number of peaks is reduced to 4 peaks (Fig. 10). Based on the number of peaks, then annealing at 600 ^{o}C presents the best result for grain growth without changing the type of crystal, and annealing at 750 ^{o}C and for crystal growth, but there is a reduction in the number of peaks on the diffractogram which means a decrease in the type of crystals which becomes 4 types. Compared to specimen from rapid quenching, specimens from annealing at 500 ^{o}C and 700 ^{o}C have the same crystallite size, which is 11.18 Å. The same prevails when compared with the number of diffractogram peaks for specimens from annealing at 500 ^{o}C which is 10 peaks, and 13 peaks for annealing at 700 ^{o}C. So, annealing at this temperature presents good results to increase the type of cystallite or for randomization, whereas the best result is obtained at annealing at 700 ^{o}C.

Dislocation density (ρ)

From Table 1, dislocation density data for specimen from rapid quenching is 1.2×10^{16} m/m^3, from annealing at 500 °C is 2.4×10^{16} m/m^3, from annealing at 600 °C is 2.7×10^{15} m/m^3, from annealing at 700 °C is 2.4×10^{16} m/m^3, from annealing at 750 °C is 6.0×10^{14} m/m^3. The crystallite size and density of specimens from rapid quenching, annealing at 600 °C and 750 °C are respectively: 15.18 Å, 33.33 Å and 70.71 Å; and 1.2×10^{16} m/m^3, 2.7×10^{15} m/m^3, and 6.0×10^{14} m/m^3. From the data, it is concluded that the greater the crystallite size, the smaller the dislocation density.

Yield Strength (Y_s)

From Table-1, the yield strength data for specimen from rapid quenching is 818.21 MPa, from annealing at 500 ^{o}C 103.40 MPa, from annealing at 600 ^{o}C 532 MPa, from annealing at 700 ^{o}C 1043.40 MPa, and from annealing at 750 ^{o}C 396.11 MPa. Comparing the yield strengths from rapid quenching, annealing at 600 ^{o}C and 750 ^{o}C, it can be seen that the yield strength tends to decrease. The correlation between stress (σ) and dislocation density (ρ) is empirically formulated as follows [13]: $\sigma = \sigma_o + k\rho^{1/2}$. This correlation is the same with equation (5) which is obtained from cystallography. The yield strengths from annealing at 500 °C and 700 °C are the same, which is 1043.40 MPa. Therefore, annealing at these temperatures is favourable for hardening or strengthening. Meanwhile, annealing at temperatures of 600 °C and 750 °C is favourable for softening or residual stress release.

Identification of Precipitates

The results of precipitate identification are not labeled in the figures because the peaks are overlapping. Based on X-ray diffraction data from the ingots, SPP Fe_2Nb is found to have a hexagonal crystal shape with lattice distances of a=1.8215 and c=7.877 with JCPDF#15–0316 as the reference. SPP is not found for the Sn element. The Law of Home Rothery[14] estimates that solid solution may form if the difference in the diameter of the dissolved atom and solvent atom is not more than 14-15%. If the diameter of the solvent atom is greater, then the dissolution is of interstitial type, and if smaller, then it is of the substitutional type. The diameters of Sn and Nb atom are almost the same as that of Zr atom. Meanwhile, Fe atom has a smaller diameter than Zr. Thus, Sn and Nb atoms are dissolved substitutionally and Fe is dissolved interstitially in the α-phase. Based on this law, the solubility of these elements in the β-phase is almost the same as that in the α-phase, which is very low. According to the phase diagram, the solubility of the elements is greater in the β-phase.

The different solubilities in the α and β-phase may be explained using the Brillouin zone theory [15]. In the α-phase, an overlap takes place on the Fermi surface whereas no overlap occurs in β-phase. The absence of other precipitates is due to the fact that most alloying elements become solid solution in the alloy ingot. According to the corresponding law, SPP that are formed has a hexagonal crystal shape with α–Zr as the matrix crystal.

After the specimens are annealed at a temperature of 400 °C, the population of SPP increases drastically. The following SPP crystals are observed: Fe_2Nb with a hexagonal crystal shape

with lattice distances of a =1.8215 and c =7.877 with JCPDF#15–0316 as the reference (angle 2θ = 56.937, 68.053, 69.523). $ZrSn_2$ with an orthorhombic crystal shape with lattice distances of a = 9.573, b = 5.644 and c = 9.927 with JCPDF # 06–0316 as the reference (angle 2θ = 33.563, 36.68, 66.287, 75.44, 76.154). $NbSn_2$ with an orthorhombic crystal shape with lattice distances of a = 19.0876, b = 5.645 and c = 9.852 with JCPDF # 19–0876 as the reference (angle 2θ =31.857, 34.564, 36.464, 56.565, 69.410, 73.067). SnZr with an orthorhombic crystal shape with lattice distances of a = 7.433,b = 5.822 and c = 5.157 with JCPDF # 10–0218 as the reference (angle 2θ = 28.428, 34.776, 36.377, 45.183, 77.112). FeSn with a hexagonal crystal shape with lattice distances of a =5.302, and c =4.449 with JCPDF # 09–0212 as the reference (angle 2θ = 56.626, 68.043, 69.459, 73.802). $Fe_2Nb_{0.4}Zr_{0.6}$ with a hexagonal crystal shape with lattice distances of a =4.927, and 24.162 with JCPDF # 23–0303 as the reference (angle 2θ = 54.796, 56,038). $Zr_{0.68}Nb_{0.25}Fe_{0.08}$ with an undetermined crystal shape with JCPDF # 17–0509 as the reference (angle 2θ = 34.495, 36.68, 47.608, 54.983).

After that, the specimens are annealed at a temperature of 500 °C, in which the population of SPP is still abundant and the disappearance of one compound, $ZrSn_2$. The following SPP crystals are observed: Fe_2Nb with a hexagonal crystal shape with lattice distances of a = 1.8215 and c = 7.877 with JCPDF#15–0316 as the reference (angle 2θ = 56.937, 68.053, 69.523). $NbSn_2$ with an orthorhombic crystal shape with lattice distances of a = 19.0876, b = 5.645 and c = 9.852 with JCPDF # 19–0876 as the reference (angle 2θ=31.857, 34.564, 36.464, 56.565, 69.410, 73.067). SnZr with an orthorhombic crystal shape with lattice distances of a =7.433, b = 5.822 and c =5.157 with JCPDF # 10–0218 as the reference (angle 2θ=28.428, 34.776, 36.377, 45.183, 77.112). FeSn with a hexagonal crystal shape with lattice distances of a = 5.302, and c = 4.449 with JCPDF # 09–0212 as the reference (angle 2θ = 56.626, 68.043, 69.459, 73.802). $Fe_2Nb_{0.4}Zr_{0.6}$ with a hexagonal crystal shape with lattice distances of a =4.927, and 24.162 with JCPDF # 23–0303 as the reference (angle 2θ = 54.796, 56.038). $Zr_{0.68}Nb_{0.25}Fe_{0.08}$ with an undetermined crystal shape with JCPDF # 17–0509 as the reference (angle 2θ = 34.495, 36.68, 47.608, 54.983).

From the specimens annealed at 600 °C, the population of SPP is still abundant and two compounds disappear, which are SnZr and $Fe_2Nb_{0.4}Zr_{0.6}$. The following SPP crystals are observed: $ZrSn_2$ with an orthorhombic crystal shape with lattice distances of a =9.573, b = 5.644 and c =9.927 with JCPDF # 06–0316 as the reference (angle 2θ = 33.563, 36,68, 66.287, 75.44, 76.154). Fe_2Nb with a hexagonal crystal shape with lattice distances of a =1.8215 and c =7.877 with JCPDF#15–0316 as the reference (angle 2θ = 56.937, 68.053, 69.523). $NbSn_2$ with an orthorhombic crystal shape with lattice distances of a =19.0876, b = 5.645 and c =9.852 with JCPDF # 19–0876 as the reference (angle 2θ=31.857, 34.564, 36.464, 56.565, 69.410, 73.067). FeSn with a hexagonal crystal shape with lattice distances of a = 5.302 and c = 4.449 with JCPDF # 09–0212 as the reference (angle 2θ = 56.626, 68.043, 69.459, 73.802). $Zr_{0.68}Nb_{0.25}Fe_{0.08}$ with undetermined crystal shape with JCPDF # 17–0509 as the reference (angle 2θ = 34.495, 36.68, 47.608, 54.983).

In the specimens annealed at 700 °C, ω–Zr is observed with a hexagonal crystal shape with lattice distances of a = 5.039 and c = 3.136 with JCPDF # 09–0212 as the reference (angle 2θ = 28.493, 35.495, 50.915, 63.832, 70.783). There is a change of phase, which is the formation of ω–Zr phase and of the type of SPP population. The following SPP crystals are observed: $ZrSn_2$ with an orthorhombic crystal shape with lattice distances of a = 9.573, b = 5.644 and c = 9.927 with JCPDF # 06–0316 as the reference (angle 2θ = 33.563, 36,68, 66.287, 75.44, 76.154). FeSn with a hexagonal crystal shape with lattice distances of a = 5.302, and c = 4.449 with JCPDF # 09–0212 as the reference (angle 2θ = 56.626, 68.043, 69.459, 73.802). Fe_2Nb with a hexagonal crystal shape with lattice distances of a = 1.8215 and c = 7.877 with JCPDF#15–0316 as the reference (angle 2θ = 56.937, 68.053, 69.523). $FeZr_2$ with a tetragonal crystal shape with lattice distances of a = 6.385 and c = 5.596 with JCPDF#25–0420 as the reference (angle 2θ = 27.946, 35.307, 40.404, 45.067, 59.136, 61.615, 70.539). $Fe_{37}Nb_9Zr_{54}$ with undetermined crystal shape with JCPDF # 46–1095 as the reference (angle 2θ = 48.443, 55.527).

For specimens annealed near the β–Zr zone at 800 °C, there is a change of phase which is the disappearance of ω–Zr phase and a number of SPP populations. The following SPP crystals are observed: FeSn with a hexagonal crystal shape with lattice distances of a = 5.302, and c = 4.449 with JCPDF # 09–0212 as the reference (angle 2θ = 56.626, 68.043, 69.459, 73.802). Fe_2Nb with a hexagonal crystal shape with lattice distances of a = 1.8215 and c = 7.877 with JCPDF#15–0316 as the reference (angle 2θ = 56.937, 68.053, 69.523).

$NbSn_2$ with an orthorhombic crystal shape with lattice distances of a = 19.0876, b = 5.645 and c = 9.852 with JCPDF # 19–0876 as the reference (angle 2θ = 31.857, 34.564, 36.464, 56.565, 69.410, 73.067).

CONCLUSIONS

Based on the results of this study, it can be concluded as follows. Ingot of Zr-Sn-Nb-Fe alloy possesses microstructure that is unstructured, which indicates the presence of Zr-Fe precipitates. After rolling, the samples do not experience cracking defects, and the twinning system seems to dominate the deformation. Heating until 750 ^oC for 2 hours does not yield perfect grain growth, which is likely due to pinning of the precipitates. Annealing at 500 ^oC and 700 ^oC is favorable for precipitation or randomization of the crystals. Annealing at a temperature of 750 °C is favorable for the growth of equiaxed grains as there are no stacking faults or precipitates which cause small microstrain. The greater the crystallite size, the smaller the dislocation density. Annealing at temperatures of 500 °C and 700 °C is suitable for hardening or strengthening. Annealing at temperatures of 600 °C and 750 ^oC is favorable for softening and residual stress release. Agreeable nucleation of SPP second-phase particles occurs at annealing temperatures of 400 °C, 500 °C, and 700 °C. In Zr-1%Nb-1% Sn-1%Fe alloy at annealing temperatures from 400 °C until 800 °C, the SPP of Fe_2Nb, $ZrSn_2$, FeSn, SnZr, $NbSn_2$, $Zr_{0.68}Nb_{0.25}Fe_{0.08}$, $Fe_2Nb_{0.4}Zr_{0.6}$, $Fe_{37}Nb_9Zr_{54}$, and ω–Zr are observed. On the whole, the study demonstrates that analysis of precipitates on zirconium-based alloys can be performed using X-ray diffraction method.

ACKNOWLEDGEMENT

The author would like to thank colleagues at PTBN-BATAN and PTBIN-BATAN for their tremendous contributions toward this work.

REFERENCES

1. J.D.B. Lambert and R. Strain, *Oxide Fuels*, in: Materials Science and Technology, Wiley - Vch, Germany Vol. **10** A (2006) 121.
2. J.E. Harbottle and A.A. Strasser, *Towards Failure-Free Fuel*, Fuel Review 1994: Design, Nuclear Engineering International (1994) 28.
3. B. Lustman and F.J.R. Kerze, The Metallurgy of Zirconium, 1st ed., Mcgraw-Hill, New York (1955) 632.
4. S. Banerjee, *Better Materials for Nuclear Energy*, IAEA Scientific Forum (2005).
5. M. Osskarson, Study on The Mechanisms For Corrosion and Hydriding of Zircaloy, Ph.D. Thesis, Royal Institute of Technology, Stockholm (2000).
6. R.T. Webster, *Zirconium and Hafnium and Their Alloys*, in: Asm Handbook Vol. 2, 10th ed., American Society For Metals (1992) 661.
7. Anonymous, Waterside Corrosion of Zirconium Alloys in Nuclear Power Plants, IAEA-TECDOC-996, IAEA, Vienna (1998).
8. T. Isobe and Y. Matsuo, *Development of Highly Corrosion Resistant Zirconium-Base Alloys*, *Zirconium in the Nuclear Industry*, 9th International Symposium, Kobe, Japan, Astm-Stp 1132, American Society for Testing and Materials, Pennsylvania (1991) 346.
9. P. George, *et. al*, *Process For Fabricating a Zirconium-Niobium Alloy and Articles Resulting Rherefrom*, US Patent 4649023 (1987).
10. B.D. Cullity, X-Ray Diffraction, Addison Wesley, London, England (1959).
11. G. Caglioti, A. Paoletti and F.P. Ricci, Nuclear Instrument Method **3** (1958) 223.
12. J.V. Sharp, M.J. Makin and J.W. Christian, Physics Status Solidi **11** (1965) 845.
13. R.E. Reed-Hill, Physical Metallurgy Principles, 2nd ed., Wadsward, California (1973) 832.
14. B. Lustman and F.J.R. Kerze, The Metallurgy of Zirconium, 1st ed., Mcgraw-Hill Inc, New York (1955) 632.
15. B.G. Parvenov, V.V. Gerasimov and G.I. Venediktova, Corrosion of Zirconium and Zirconium Alloys, Atomizdat, Moskva **23** (1967).